

# Pulsed plasma chemical synthesis of Fe<sub>2</sub>O<sub>3</sub>@TiO<sub>2</sub> core-shell nanocomposites

Galina Kholodnaya<sup>1</sup> ✉, Roman Sazonov<sup>1</sup>, Denis Ponomarev<sup>1</sup>, Alexander Sivkov<sup>1</sup>, Ivan Shanenkov<sup>1</sup>, Fedor Konusov<sup>1</sup>, Ruslan Gadirov<sup>2</sup>

<sup>1</sup>Tomsk Polytechnic University, 30 Lenin Avenue, Tomsk, Russia

<sup>2</sup>Siberian Physical-Technical Institute, Tomsk State University, 1 Novosobornaya Sq., Tomsk, Russia

✉ E-mail: galina\_kholodnaya@mail.ru

Published in Micro & Nano Letters; Received on 21st February 2020; Revised on 14th May 2020; Accepted on 31st May 2020

The Letter presents the results of the experimental investigation on the synthesis of core-shell structured nanocomposites. Iron oxide, which served as a nucleus in the composite, was synthesised using the plasma dynamic method. The composite shell was titanium oxide produced by the pulsed plasma chemical method. Average sizes of nanoparticles were estimated between 50 and 150 nm in the Fe<sub>2</sub>O<sub>3</sub>@TiO<sub>2</sub> core-shell structured composite nanoparticles using TEM. A distinctive feature of the morphology of the synthesised Fe<sub>2</sub>O<sub>3</sub>@TiO<sub>2</sub> core-shell is that the core entirely encapsulates clusters of titanium oxide nanoparticles. The wall thickness of the coating is 5–10 nm. The spectral dependence of the absorption coefficient  $\alpha(h\nu)$  was calculated for the Fe<sub>2</sub>O<sub>3</sub>@TiO<sub>2</sub> composite. The interband absorption parameters are determined in the energy intervals  $\Delta'(h\nu)$  upon approximation of the absorption spectra. The bandgap for indirect and direct allowed transitions is 1.36 and 1.97 eV for  $E_g''$  and  $E_g'$ , respectively.

**1. Introduction:** The synthesis methods and properties of nanoparticles with a core-shell structure have attracted much attention from many research groups. The fusion of individual particles into a single system makes it possible to improve the physicochemical properties of nanocomposites (morphology, size, optical, magnetic, and electrical characteristics) and expand applications, including biomedical applications [1–3], electronics [4, 5], and catalysis [6–8]. The properties of core-shell nanocomposites can vary due to changes in the material of the core or shell or the ratio of the sizes of the core and shell.

One of the promising nanocomposites with a core-shell structure is the Fe<sub>2</sub>O<sub>3</sub>@TiO<sub>2</sub> composite. Titanium oxide is a semiconductor whose nanoparticles have a higher photocatalytic effect than microparticles. TiO<sub>2</sub> nanoparticles form reactive oxygen species, hydroxyl radicals etc., under the influence of ultraviolet (UV) radiation. The photocatalytic effect is also observed when exposed to visible light when single-layered TiO<sub>2</sub> nanoparticles were doped into carbon structures [9, 10] or onto the surface of iron oxide [11–14]. The recombination rate of photogenerated electrons and holes increased in the synthesised Fe<sub>2</sub>O<sub>3</sub>@TiO<sub>2</sub> core-shell nanocomposite [11–17]. Chen *et al.* [11] used a combined method based on solvothermal and sol-gel methods to produce the spherical Fe<sub>2</sub>O<sub>3</sub>@TiO<sub>2</sub> nanocomposites. The photocatalytic activity of the composite was studied by decomposition of methylene blue (MB) under the influence of UV and visible light. The observed photocatalytic characteristics of Fe<sub>2</sub>O<sub>3</sub>@TiO<sub>2</sub> nanospheres are explained by the synergistic effects of the core-shell structure, which indicates that the TiO<sub>2</sub> shell improves the photocatalytic characteristics of  $\alpha$ -Fe<sub>2</sub>O<sub>3</sub>. Xia and Yin [12] studied the effect of the core-shell-volume ratio on the photocatalytic activity during the decomposition of Rhodamine B fluorescent dye. These authors were able to reduce the recombination rate of photogenerated electrons and holes and organise the operation of the Fe<sub>2</sub>O<sub>3</sub>@TiO<sub>2</sub> photocatalyst in the visible light region by changing Fe<sub>2</sub>O<sub>3</sub>/TiO<sub>2</sub> molar ratios. Chen *et al.* [14] found that the thickness and crystal structure of TiO<sub>2</sub> affect the photocatalytic activity of Fe<sub>2</sub>O<sub>3</sub>@TiO<sub>2</sub> nanocomposites. In [15], the effect of particle morphology on the photocatalytic properties of Fe<sub>2</sub>O<sub>3</sub>@TiO<sub>2</sub> nanocomposites was studied. The particles in the form of disks with roughnesses had high photocatalytic activity compared to particles of a round and smooth shape. Kim *et al.* [16] examined the effect of

calcination temperature (500–800°C) during sol-gel synthesis on the photocatalytic activity of the Fe<sub>2</sub>O<sub>3</sub>@TiO<sub>2</sub> composite. The Fe<sub>2</sub>O<sub>3</sub>@TiO<sub>2</sub> composite produced at a temperature of 700°C showed higher photocatalytic activity than Fe<sub>2</sub>O<sub>3</sub>@TiO<sub>2</sub> at 500°C.

It is well known that the magnetic properties of a material depend on its size to a large extent. For sizes from 20 to 1000 nm, the magnetic characteristics strongly depend on the background of the sample, i.e. the method of its preparation. Encapsulation using a pulsed plasma-chemical method makes it possible to produce nanostructures avoiding liquid components. This can positively affect the conservation of the magnetic properties of the nuclei.

The aim of this work was to synthesise Fe<sub>2</sub>O<sub>3</sub>@TiO<sub>2</sub> core-shell structured nanocomposites, in which Fe<sub>2</sub>O<sub>3</sub> is a core, while TiO<sub>2</sub> is a shell, as well as to study physicochemical properties (morphology, size, and crystal structure) and to calculate the bandgap of the synthesised Fe<sub>2</sub>O<sub>3</sub>@TiO<sub>2</sub> composites. The use of a pulsed plasma-chemical method for the synthesis of Fe<sub>2</sub>O<sub>3</sub>@TiO<sub>2</sub> nanocomposites seems promising due to the fact that this method has (i) high-energy stress of the system, which causes high temperatures and, therefore, high rates of chemical reactions that reduces the size of chemical reactors; (ii) the presence of significant concentrations of active particles (radicals, excited molecules, and ions) in plasma, which, with their participation in chain processes, can significantly accelerate many chemical reactions; (iii) production of the product in a single-step process in most cases; (iv) production of nanocomposites with varied properties due to synthesis modes; (v) the universality of the method, i.e. using the same equipment it is possible to synthesise nanocomposites with different chemical, phase, morphological composition.

**2. Experimental details: preparation of Fe<sub>2</sub>O<sub>3</sub> particles and synthesis of Fe<sub>2</sub>O<sub>3</sub>@TiO<sub>2</sub> core-shell nanoparticles:** The Fe<sub>2</sub>O<sub>3</sub>@TiO<sub>2</sub> nanocomposites were synthesised in two stages. In the first stage, the Fe<sub>2</sub>O<sub>3</sub> nuclei were synthesised by the plasma dynamic method. The second stage involved creating a core-shell composite by coating Fe<sub>2</sub>O<sub>3</sub> particles with TiO<sub>2</sub> using the plasma chemical method.

To synthesise Fe<sub>2</sub>O<sub>3</sub> particles, we used steel grade St 10. Gaseous technical oxygen (purity 99.9%) served as a precursor to oxygen. A shell of TiO<sub>2</sub> was coated using titanium tetrachloride (TiCl<sub>4</sub>, 99.9%), oxygen (O<sub>2</sub>, 99.9%), and hydrogen (H<sub>2</sub>, 99.9%).

For the first stage, the experimental setup for the plasma dynamic synthesis of iron oxides includes three main blocks. The first block is a sectioned capacitive energy storage device. The second block is a high-voltage high-current pulsed coaxial magnetoplasma accelerator with iron electrodes and an accelerating channel. The third block is the working chamber (reactor) [18, 19]. A capacitive energy storage device is charged to a certain value, and then it is discharged to the electrodes of a high-voltage high-current pulsed coaxial magnetoplasma accelerator. An arc discharge arises in the interelectrode gap; as a result, electroerosion produces iron from the surface of the electrodes in the working medium (oxygen). Hence, iron is oxidised followed by crystallisation and formation of iron oxide particles with a high content of epsilon phase  $\epsilon\text{-Fe}_2\text{O}_3$  (up to 90 wt%) [18, 19]. The average size of iron oxide particles ranged between 50 and 100 nm.

At the second stage, a titanium oxide shell was coated on the synthesised  $\text{Fe}_2\text{O}_3$  particles by the plasma chemical method. A TEA-500 pulsed electron accelerator [20, 21] and a reaction chamber (quartz tube, 16 cm diameter, 6 l volume) were used for the plasma chemical synthesis method. The  $\text{Fe}_2\text{O}_3$  particles were placed in a plasma chemical reactor (Fig. 1).

A pulsed electron beam was injected into the plasma chemical reactor filled with initial reagents ( $\text{TiCl}_4$ ,  $\text{O}_2$ ,  $\text{H}_2$ , and  $\text{Fe}_2\text{O}_3$  particles). The energy of the electron beam was introduced into the mixture; as a result, non-equilibrium plasma arises followed by chemical reactions, the products of which are nanoscale composites. Volumetric excitation of the reaction gas occurs by a pulsed electron beam, and the process of reactions proceeds in the entire excitation region. As a result, studies showed that the  $\text{Fe}_2\text{O}_3@\text{TiO}_2$  core-shell structured spherical nanoparticles were synthesised.

**Characterisations:** The morphology of the  $\text{Fe}_2\text{O}_3@\text{TiO}_2$  composite nanoparticles was studied using the JEOL-II-100 transmission electron microscope (Jeol Ltd, Japan). X-ray diffraction patterns of the synthesised  $\text{Fe}_2\text{O}_3@\text{TiO}_2$  nanocomposites were obtained using a Shimadzu XRD 7000S X-ray diffractometer (Shimadzu, Japan) with  $\text{CuK}\alpha$  radiation in the  $2\theta$  mode at a scanning speed of  $0.01\text{ s}^{-1}$ . Using the AvaSpec-2048-2 spectrometer (Avantes) with the AvaLight-DHS light source (deuterium and halogen-tungsten lamps) and an integrating sphere, the spectral dependences of the diffuse reflection coefficient  $R(h\nu)$  of the powders were measured.

**3. Results and discussion: morphology and composition:** The morphological features of the  $\text{Fe}_2\text{O}_3@\text{TiO}_2$  composite nanoparticles based on the obtained TEM images are shown in Fig. 2.

Fig. 2 shows that the  $\text{Fe}_2\text{O}_3@\text{TiO}_2$  composite nanoparticles have a smooth surface, a regular spherical shape without any cavities. The average particle size is in the range of 40–80 nm (Fig. 2a). Some particles with an average size of 40–60 nm are combined into agglomerates in the form of elongated ovals. A thin shell with a thickness of 7–9 nm, which tightly covers individual particles, can be seen (Fig. 2b). In addition, the shell is also observed

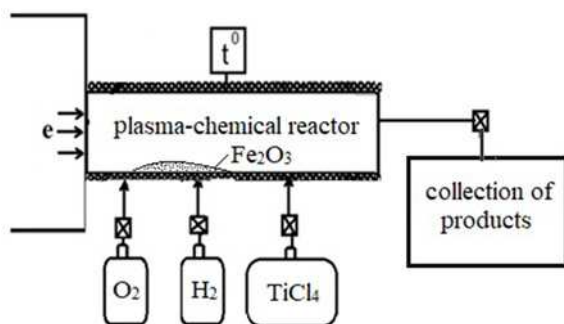


Fig. 1 Experimental design

in the accumulation of particles (Fig. 2a). The shell thickness does not exceed 10 nm. Large particles with an average size of  $>200\text{ nm}$  are found (Fig. 2a).

Fig. 3 shows a TEM image with specifically identified points (15, 16) with their characteristic nanodiffraction patterns.

The SAED pattern obtained from the core of the composite particle (point 15) has the form characteristic of single crystals of the epsilon phase of iron oxide with the orthorhombic unit cell in the zone axis pattern [001] identical to that reported in [22]. This suggests that the core of the particles is iron oxide. The SAED pattern from the selected region 16 (the shell of a characteristic composite particle) has a point nature. Most reflexes with sufficiently high accuracy for determining the interplanar spacing for this method of phase microanalysis correspond to the structural model of  $\text{TiO}_2$  rutile (JCPDS 00-21-1276). The presence of brightly visible reflexes indicates the crystal structure of such shells. The presence of reflections from the crystal planes of the epsilon phase of iron oxide can be explained by the fact that the electron beam most likely passed through the core material.

Fig. 4 shows the colour windows of the corresponding chemical elements for the  $\text{Fe}_2\text{O}_3@\text{TiO}_2$  nanocomposites obtained using the EDX method.

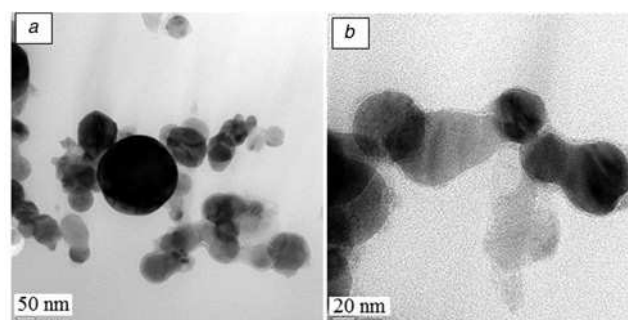


Fig. 2 TEM images of the  $\text{Fe}_2\text{O}_3@\text{TiO}_2$  composite

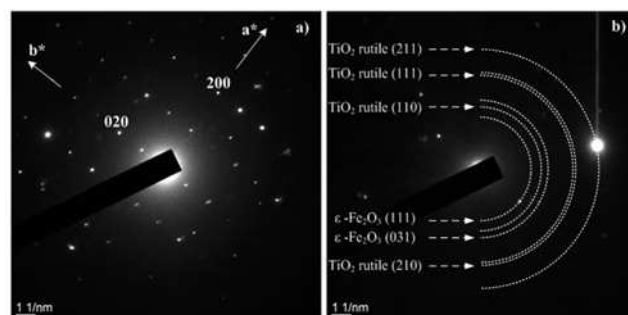
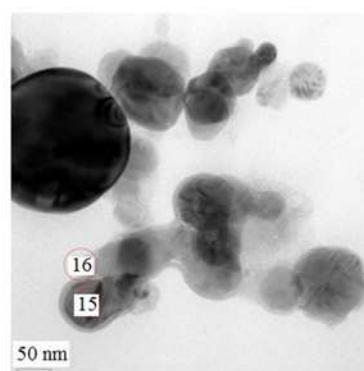


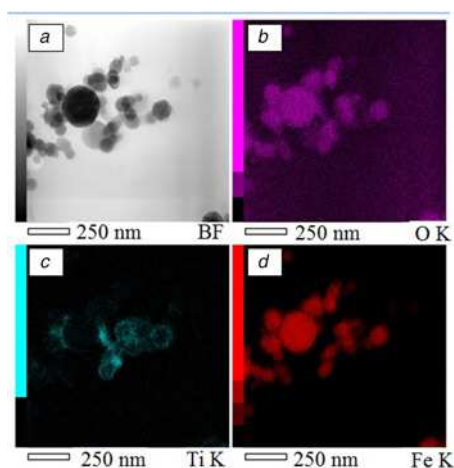
Fig. 3 TEM image of the synthesised  $\text{Fe}_2\text{O}_3@\text{TiO}_2$  particles and their nanodiffraction patterns

Fig. 4 shows that the nanocomposite consists of an iron oxide core coated with a titanium-containing shell. Only the particles whose size does not exceed 60 nm are coated with a shell of titanium oxide. Fig. 4c shows that titanium is located on the surface, because there are voids inside the particle, while in Figs. 4b and d these voids are designated as elements of iron and oxygen. In addition, it is seen that not all particles are coated with titanium particles. There is a part of the particles representing iron oxide, which indicates incomplete capsulation of all particles.

Figs. 5a and b present XRD patterns of the synthesised  $\text{Fe}_2\text{O}_3@\text{TiO}_2$  composite nanoparticles and  $\text{Fe}_2\text{O}_3$  particles.

Comparing the XRD patterns in Figs. 5a and b, it can be seen that they are almost identical. The lines obtained for the  $\text{Fe}_2\text{O}_3@\text{TiO}_2$  nanocomposite are consistent with the position of the lines of the database of XRD patterns for  $\epsilon\text{-Fe}_2\text{O}_3$  and  $\alpha\text{-Fe}_2\text{O}_3$ , indicating a high phase uniformity of the produced particles with the dominance of the epsilon phase of iron oxide in the product.

Using the Scherrer equation, the sizes of coherent scattering regions were calculated for the crystalline phases  $\epsilon\text{-Fe}_2\text{O}_3$  and haematite  $\alpha\text{-Fe}_2\text{O}_3$ . For  $\epsilon\text{-Fe}_2\text{O}_3$ , the crystallite sizes did not exceed 13.8 nm, while for haematite  $\alpha\text{-Fe}_2\text{O}_3$  they were 26.6 nm. The contents of  $\epsilon\text{-Fe}_2\text{O}_3$  and haematite  $\alpha\text{-Fe}_2\text{O}_3$  were 79 and 21%, respectively.



**Fig. 4** TEM image of the synthesised  $\text{Fe}_2\text{O}_3@\text{TiO}_2$  particles  
a Colour windows reflecting the elements (oxygen)  
b Titanium  
c Iron  
d Of the  $\text{Fe}_2\text{O}_3@\text{TiO}_2$  sample

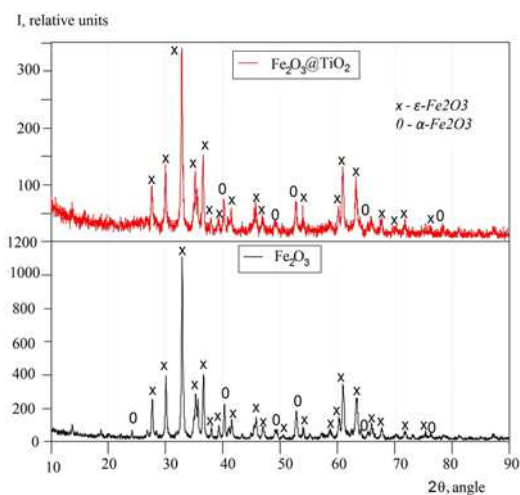


**Fig. 5** XRD patterns of the samples of the  $\text{Fe}_2\text{O}_3@\text{TiO}_2$  composites

In addition, when analysing diffraction patterns with a large step along the  $2\theta$  axis, a peak (36.2) was observed for the composite powder, which can be attributed to the peak of the corresponding crystal lattice characteristic of rutile titanium oxide, which also confirms the results of TEM on the formation of the oxide–titanium shell with a crystalline structure on iron oxide particles (Fig. 6).

The weak intensity of this maximum and the absence of other reflections of the crystalline planes of titanium oxide can be caused by the small size of the shells, which give weak reflections compared to the large particles of iron oxide.

**Optical property:** To determine the interband absorption characteristics for the  $\text{Fe}_2\text{O}_3@\text{TiO}_2$  composite, the diffuse reflection method was used [23, 24]. The spectral dependence of the diffuse reflection coefficient  $R(h\nu)$  for the  $\text{Fe}_2\text{O}_3@\text{TiO}_2$  nanocomposite was measured. Then, the spectral dependence of the absorption coefficient  $\alpha(h\nu)$  (Fig. 7) was calculated using the reflection spectra by (1) [23]

$$\alpha(h\nu) = A \cdot (1 - R(h\nu))/R(h\nu) \quad (1)$$

The absorption spectra  $\alpha(h\nu)$  were approximated by the Urbach rule to determine the absorption parameters using the localised states of defects distributed in the bandgap of the material [23].

The interband absorption parameters are determined in the energy intervals  $\Delta'(h\nu)$  upon approximation of the absorption

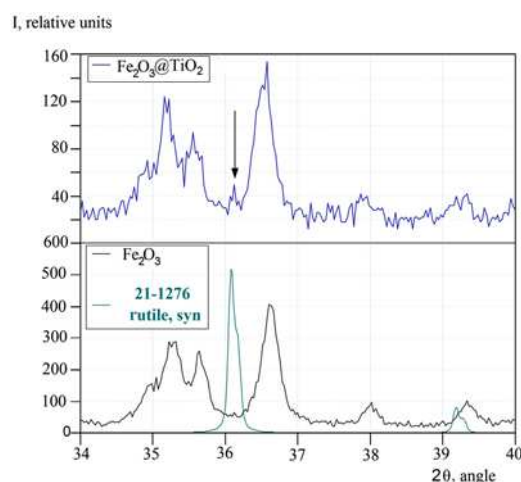


**Fig. 6** XRD patterns of the samples of the  $\text{Fe}_2\text{O}_3@\text{TiO}_2$  composites, obtained when analysing diffraction patterns with a large step along the  $2\theta$  axis

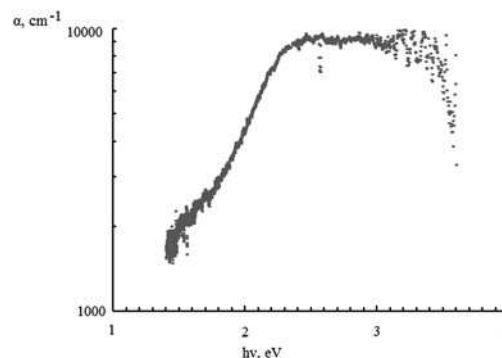


**Fig. 7** Interband absorption in a model developed for the absorption of amorphous semiconductors in the  $\text{Fe}_2\text{O}_3@\text{TiO}_2$  powder

spectra by a power law

$$\alpha \cdot h\nu \sim (h\nu - E_g'')^m, \quad (2)$$

where  $m = 1/2$  and 2 correspond to direct and indirect interband allowed transitions through the optical gap for the direct  $E_g'$  and indirect  $E_g''$  transitions.

Thus, the spectral dependence of the absorption coefficient  $\alpha(h\nu)$  was calculated for the  $\text{Fe}_2\text{O}_3/\text{TiO}_2$  sample. The optical transmission of 2.5–4 rel. un. is characteristic. The interband absorption parameters are determined in the energy intervals  $\Delta'(h\nu)$  upon approximation of the absorption spectra. The bandgap is for indirect and direct allowed transitions for  $E_g'' = 1.36$  eV and  $E_g' = 1.97$  eV. It should be noted that titanium oxide is a wide-gap indirect-type semiconductor. The experimental data also indicate a shift in the absorption edge to red and the appearance of absorption in the visible region. The most probable reason for the observed absorption in the visible region is the presence of the  $\epsilon\text{-Fe}_2\text{O}_3$  nucleus in the samples.

We have investigated  $\text{Fe}_2\text{O}_3/\text{TiO}_2$  powders for their applicability as electrocatalysts. The studies were performed in an undivided cell (the working electrode is a glass graphite disk with a visible area of  $0.03\text{ cm}^2$ ; the auxiliary electrode is a platinum grid; the reference electrode is  $\text{Ag}/\text{AgCl}$ ) using a computerised electrochemical complex based on PI-50-1 potentiostat. A solution of  $\text{H}_2\text{SO}_4$  and  $\text{NaOH}$  was used as an electrolyte. The electrocatalyst was applied to the electrode surface in the form of a mass based on acetylene black, a binder (water emulsion of fluoroplastic), and a nanocomposite. The measurement error of the electrochemical characteristics was  $\pm 5\%$ . The  $\text{Fe}_2\text{O}_3/\text{TiO}_2$  sample showed weak electrocatalytic properties. This is probably due to the high recombination rate of the main charge carriers in  $\text{Fe}_x\text{O}_y\text{-TiO}_2$ . Additives of precious metals can reduce the rate of recombination and pull electrons onto themselves from the bulk of the material. Perhaps combinations such as  $\text{Au}/\text{Fe}_2\text{O}_3$ ,  $\text{Ag}/\text{Fe}_2\text{O}_3$ ,  $\text{Pt}/\text{Fe}_2\text{O}_3$ ,  $\text{Au}/\text{TiO}_2$ ,  $\text{Ag}/\text{TiO}_2$ ,  $\text{Pt}/\text{TiO}_2$ ,  $\text{Ag}/\text{Fe}_2\text{O}_3/\text{TiO}_2$  etc. can show significantly greater activity.

**4. Conclusion:** A two-stage method was used to synthesise the  $\text{Fe}_2\text{O}_3/\text{TiO}_2$  nanocomposite. It was found that the produced composite consists of  $\text{Fe}_2\text{O}_3$  particles, which have a spherical shape and form a core coated with a titanium oxide shell of a thickness of about 7–10 nm. The particle size of the nanocomposite with a core-shell structure is 40–60 nm. The phase composition of the nanocomposite is a mixture of the crystalline phase characteristic of titanium oxide (rutile) and iron oxide, presented as  $\alpha\text{-Fe}_2\text{O}_3$  and  $\epsilon\text{-Fe}_2\text{O}_3$ . The bandgap for indirectly allowed transitions (1.36 eV) is obtained for the synthesised  $\text{Fe}_2\text{O}_3/\text{TiO}_2$  composite.

**5. Acknowledgments:** This work was supported by the Russian Science Foundation, research project no. 18-73-10011. The optimisation of the plasma-dynamic synthesis system and corresponding method, as well as producing iron oxide powders with a high content of the epsilon phase was supported by the Russian Foundation for Basic Research (project no. 19-42-703007).

## 6 References

- [1] Rabie H., Zhang Y., Pasquale N., *ET AL.*: 'NIR biosensing of neurotransmitters in stem cell-derived neural interface using advanced core-shell upconversion nanoparticles', *Adv. Mater.*, 2019, **31**, (14), 1806991, doi:10.1002/adma.201806991
- [2] Chen Y., Li J., Yuan Z., *ET AL.*: 'Metabolic fate and subchronic biological effects of core-shell structured  $\text{Fe}_3\text{O}_4/\text{SiO}_2\text{-NH}_2$  nanoparticles', *Nanotoxicology*, 2018, **12**, (6), pp. 621–636
- [3] Zhang L., Yang Z., Zhu W., *ET AL.*: 'Dual-stimuli-responsive, polymer-microsphere-encapsulated  $\text{CuS}$  nanoparticles for magnetic resonance imaging guided synergistic chemo-photothermal therapy', *J. Mater. Sci.*, 2017, **3**, (8), pp. 1690–1701
- [4] Fu H., Sun S., Yang X., *ET AL.*: 'A facile coating method to construct uniform porous  $\alpha\text{-Fe}_2\text{O}_3/\text{TiO}_2$  core-shell nanostructures with enhanced solar light photocatalytic activity', *Powder Technol.*, 2018, **328**, pp. 389–396
- [5] Li Y., Wei X., Zhu B., *ET AL.*: 'Hierarchically branched  $\text{Fe}_2\text{O}_3/\text{TiO}_2$  nanorod arrays for photoelectrochemical water splitting: Facile synthesis and enhanced photoelectrochemical performance', *Nanoscale*, 2016, **8**, (21), pp. 11284–11290
- [6] Liu C., Dong H., Ji Y., *ET AL.*: 'High-performance hydrogen evolution reaction catalysis achieved by small core-shell copper nanoparticles', *J. Colloid Interface Sci.*, 2019, **551**, pp. 130–137
- [7] Qin H., Wang B., Zhang C., *ET AL.*: 'Lignin based synthesis of graphitic carbon-encapsulated iron nanoparticles as effective catalyst for forming lower olefins via Fischer-Tropsch synthesis', *Catal. Commun.*, 2016, **96**, pp. 28–31
- [8] Plodinec M., Gajović A., Jakša G., *ET AL.*: 'High-temperature hydrogenation of pure and silver-decorated titanate nanotubes to increase their solar absorbance for photocatalytic application', *J. Alloys Compd.*, 2014, **591**, pp. 147–155
- [9] Cheng Q.P., Zhao N., Lyu S.S., *ET AL.*: 'Tuning interaction between cobalt catalysts and nitrogen dopants in carbon nanospheres to promote Fischer-Tropsch synthesis', *Appl. Catal. B, Environ.*, 2019, **248**, pp. 73–83
- [10] Mo Z., Xu H., Chen Z.G., *ET AL.*: 'Self-assembled synthesis of defect-engineered graphitic carbon nitride nanotubes for efficient conversion of solar energy', *Appl. Catal. B, Environ.*, 2018, **225**, pp. 154–161
- [11] Chen F.-X., Fan W.-Q., Zhou T.-Y., *ET AL.*: 'Core-shell nanospheres ( $\text{HP-Fe}_2\text{O}_3/\text{TiO}_2$ ) with hierarchical porous structures and photocatalytic properties', *Acta. Phys. Sin.*, 2013, **29**, (1), pp. 167–175
- [12] Xia Y., Yin L.: 'Core-shell structured  $\alpha\text{-Fe}_2\text{O}_3/\text{TiO}_2$  nanocomposites with improved photocatalytic activity in the visible light region', *Phys. Chem. Chem. Phys.*, 2013, **15**, (42), pp. 18627–18634
- [13] Tian X., Yin Y., Wang B., *ET AL.*: 'Anisotropic  $\alpha\text{-Fe}_2\text{O}_3/\text{TiO}_2$  core-shell nanoparticles and their smart electrorheological response', *Eur. J. Inorg. Chem.*, 2015, **3**, pp. 430–440
- [14] Chen M., Shen X., Wu Q., *ET AL.*: 'Template-assisted synthesis of core-shell  $\alpha\text{-Fe}_2\text{O}_3/\text{TiO}_2$  nanorods and their photocatalytic property', *J. Mater. Sci.*, 2013, **50**, (11), pp. 4083–4094
- [15] Liu J., Yang S., Wu W., *ET AL.*: '3D flowerlike  $\alpha\text{-Fe}_2\text{O}_3/\text{TiO}_2$  core-shell nanostructures: general synthesis and enhanced photocatalytic performance', *ACS Sustain. Chem. Eng.*, 2015, **3**, (11), pp. 2975–2984
- [16] Kim S.-E., Woo J.-Y., Kang S.-Y., *ET AL.*: 'A facile general route for ternary  $\text{Fe}_2\text{O}_3/\text{TiO}_2/\text{nanometal}$  ( $\text{Au}$ ,  $\text{Ag}$ ) composite as a high-performance and recyclable photocatalyst', *J. Ind. Eng. Chem.*, 2016, **43**, pp. 142–149
- [17] Fu Y., Wei Q., Lu B., *ET AL.*: 'Stem-like nano-heterostructural  $\text{MWCNTs}/\alpha\text{-Fe}_2\text{O}_3/\text{TiO}_2$  composite with high lithium storage capability', *J. Alloys Compd.*, 2016, **684**, pp. 419–427
- [18] Sivkov A., Naiden E., Ivashutenko A., *ET AL.*: 'Plasma dynamic synthesis and obtaining ultrafine powders of iron oxides with high content of  $\epsilon\text{-Fe}_2\text{O}_3$ ', *J. Magn. Magn. Mater.*, 2018, **405**, pp. 158–168
- [19] Shanenkov I., Sivkov A., Ivashutenko A., *ET AL.*: 'High-energy plasma dynamic synthesis of multiphase iron oxides containing  $\text{Fe}_3\text{O}_4$  and  $\epsilon\text{-Fe}_2\text{O}_3$  with possibility of controlling their phase composition', *J. Alloys Compd.*, 2019, **774**, pp. 637–645
- [20] Remnev G.E., Furman E.G., Pushkarev A.I., *ET AL.*: 'A high-current pulsed accelerator with a matching transformer', *Instrum. Exp. Tech.*, 2004, **47**, (3), pp. 394–398
- [21] Sazonov R.V., Kholodnaya G.E., Ponomarev D.V., *ET AL.*: 'Pulsed plasma chemical synthesis of carbon-containing titanium oxide-based composite', *Fullerenes, Nanotubes, Carbon Nanostructures*, 2017, **25**, (9), pp. 526–530
- [22] Kelm K., Mader W.: 'Synthesis and structural analysis of  $\epsilon\text{-Fe}_2\text{O}_3$ ', *Z. Anorg. Allg. Chem.*, 2005, **631**, (12), pp. 2383–2389
- [23] Kabyshev A.V., Konusov F.V., Remnev G.E.: 'Optical properties of  $\text{GaAs}$  films deposited via pulsed ion ablation', *J. Surf. Invest. X-ray, Synchrotron Neutron Tech.*, 2011, **5**, (2), pp. 228–235
- [24] O'Leary S.K., Zukotynski S., Perz J.M.: 'Optical absorption in amorphous semiconductors', *Phys. Rev. B*, 1995, **52**, (11), pp. 7795–7797